Iida et al. *NPG Asia Materials* (2021)13:68
https://doi.org/10.1038/s41427-021-00337-5

ARTICLE Open Access

Approaching the ultimate superconducting properties of (Ba,K)Fe_2As_2 by naturally formed low-angle grain boundary networks

Kazumasa Iida[1,2], Dongyi Qin[3], Chiara Tarantini[4], Takafumi Hatano[1,2], Chao Wang[5], Zimeng Guo[6,2], Hongye Gao[5], Hikaru Saito[7,2], Satoshi Hata[5,6,2], Michio Naito[3,2] and Akiyasu Yamamoto[3,2]

Abstract

The most effective way to enhance the dissipation-free supercurrent in the presence of a magnetic field for type II superconductors is to introduce defects that act as artificial pinning centers (APCs) for vortices. For instance, the in-field critical current density of doped $BaFe_2As_2$ (Ba122), one of the most technologically important Fe-based superconductors, has been improved over the last decade by APCs created by ion irradiation. The technique of ion irradiation has been commonly implemented to determine the ultimate superconducting properties. However, this method is rather complicated and expensive. Here, we report a surprisingly high critical current density and strong pinning efficiency close to the crystallographic *c*-axis for a K-doped Ba122 epitaxial thin film without APCs, achieving performance comparable to ion-irradiated K-doped Ba122 single crystals. Microstructural analysis reveals that the film is composed of columnar grains with widths of approximately 30–60 nm. The grains are rotated around the *b*- (or *a*-) axis by 1.5° and around the *c*-axis by −1°, resulting in the formation of low-angle grain boundary networks. This study demonstrates that the upper limit of in-field properties reached in ion-irradiated K-doped Ba122 is achievable by grain boundary engineering, which is a simple and industrially scalable manner.

Introduction

Significant progress in the growth of Fe-based superconductor (FBS) thin films has been achieved over the past decade. As a result, high-quality, epitaxial thin films of technologically important FBS [e.g., Fe(Se, Te), doped $AeFe_2As_2$ (Ae: alkaline earth elements) and doped LnFeAsO (Ln: lanthanoid elements)] are realized on different kinds of single-crystalline substrates and technical substrates[1–5] except for (Ba,K)Fe_2As_2 (K-doped Ba122). The realization of epitaxial K-doped Ba122 has been challenging due to the difficulty in controlling volatile potassium. We have recently succeeded in growing K-doped Ba122 epitaxial thin films on fluoride substrates[6], which gives a great opportunity to investigate their electrical transport properties. Our preliminary study shows that grain boundaries (GBs) are present in K-doped Ba122 despite no sign of weak-link behaviors.

GB with a misorientation angle larger than the critical angle $\theta_c \sim 9°$ becomes a detrimental defect to the critical current for most FBS[3,7,8]. On the other hand, GBs with a small misorientation angle less than θ_c do not impede the supercurrent flow. Rather, dislocation arrays in low-angle GBs (LAGBs) contribute to flux pinning[3,7,8], leading to improvements in the critical current properties of FBS thin films. Indeed, several studies have shown a proof of principle of this concept by growing P- and Co-doped Ba122 thin films on technical substrates with oxide buffer layers having a different in-plane spread prepared by ion

Correspondence: Kazumasa Iida (iida@mp.pse.nagoya-u.ac.jp)
[1]Department of Materials Physics, Nagoya University, Furo-cho, Nagoya 464–8603, Japan
[2]JST CREST, Kawaguchi, Saitama 332–0012, Japan
Full list of author information is available at the end of the article

beam-assisted deposition (IBAD)[9,10]. In both compounds, the larger the texture spread of Ba122 within θ_c, the higher the critical current density J_c, typically a few MA cm^{-2} at 4 K. Additionally, J_c for the applied field parallel to the crystallographic c-axis ($H||c$) is similar to or even higher than that for $H||ab$[10,11]. It was later demonstrated that enhanced pinning performance is due to LAGBs acting as flux pinning centers[12].

However, other well-known techniques, such as irradiation with protons and heavy ions, produce either isotropic or anisotropic defects (i.e., artificial pinning centers, APCs) significantly enhanced J_c above the value obtained by the aforementioned GB engineering. For instance, a SmFeAs(O,F) single crystal with columnar defects produced by heavy-ion irradiation exhibits a high self-field J_c of 18–20 MA cm^{-2} at 5 K, which is approximately 9–10 times the J_c of the pristine sample[13]. Similarly, $Ba_{0.6}K_{0.4}Fe_2As_2$ single crystals with point defects created by 3-MeV proton irradiation show a self-field J_c of 11 MAcm^{-2} at 2 K, which is ~4.6 times the J_c of the pristine sample[14]. Recently, a $Ba_{0.6}K_{0.4}Fe_2As_2$ single crystal irradiated by 320-MeV Au ions shows a very high self-field J_c of over 20 MA cm^{-2} at 2 K[15], corresponding to a 12% depairing current density J_d~166 MA cm^{-2}[16].

Here, we report a surprisingly high self-field J_c of 14.4 MA cm^{-2} at 4 K and a strong pinning efficiency close to the crystallographic c-axis for the K-doped Ba122 epitaxial thin film with LAGB networks. The pinning force density F_p for $H||c$ exceeds 200 GN m^{-3} at 4 K and above 6 T, which is at a level comparable to the K-doped Ba122 single crystal with Pb-ion irradiation[17].

Materials and methods

Thin film growth

K-doped Ba122 thin films were grown on CaF_2(001) at 395 °C, a slightly lower temperature than in our previous investigation, by custom designed molecular beam epitaxy using solid sources of Fe, As, Ba and In-K alloy[6]. Here, we used an In–K alloy rather than pure K because of the good controllability of the K content in the film as well as safety issues. The CaF_2 substrate was fixed on the sample holder using Ag paste to ensure good thermal conduction. Prior to deposition, the substrate was heated to 600 °C, kept at this temperature for 15 min for thermal cleaning, and subsequently cooled to 395 °C. The compositions of all fluxes except for As were monitored in situ by electron impact emission spectrometry (Ba and Fe) and atomic absorption spectrometry (K). The obtained real-time information was fed back to a personal computer that controls the proportional–integral–differential (PID) of the resistive heaters. The As flux was provided constantly during growth. Compared with our previous films, the growth parameters (i.e., deposition temperature and evaporation rate for each flux) were fully optimized, as evidenced in Supplementary Fig. S1. Unlike our previous investigation, no impurity phases were observed. Additionally, the average full width at half maximum value of the 103 ϕ-scan is 1.1°, which is smaller than our previous film[6].

Microstructural analysis by transmission electron microscopy

Cross-sectional samples were prepared by a focused ion beam. Scanning transmission electron microscopy observations were performed by a TEM (JEOL ARM-200F) operated at an acceleration voltage of 200 kV. TEM-based scanning precession electron diffraction (PED) analysis was performed by TEM (Thermo Fisher Scientific Tecnai G2 F20 equipped with NanoMEGAS ASTAR system) operated at an acceleration voltage of 200 kV. Details of crystal orientation mapping based on PED are described in ref. [18]. In this PED analysis, the convergence semiangle of the incident electron beam was 1 mrad, and the precession angle was 0.55°. The crystal orientation at each measurement point was determined by matching the PED pattern with template patterns pregenerated from the crystal structural data of K-doped Ba122[19] and CaF_2[20]. β and γ are defined as the angles between [001]CaF_2 and [001]K-doped Ba122 and [100] (or [010]) CaF_2 and [100] (or [010]) K-doped Ba122, respectively. Note that the β and γ values in this measurement include an uncertainty of ~0.4°, which was estimated from the standard deviation of crystal orientation determination on the CaF_2 substrate.

Electrical transport measurements

A small bridge 38 μm wide and 1 mm long was fabricated by laser cutting. The sample was mounted on a rotator holder in the maximum Lorentz force configuration. The angle θ is measured from the crystallographic ab-plane. Current–Voltage (I–V) characteristics were measured by a 4-probe method in a commercial physical property measurement system [(PPMS) Quantum Design]. The upper critical fields H_{c2} were defined as 90% of the normal state resistivity. The irreversibility fields H_{irr} were defined as the intersection between the resistivity traces and the resistivity criterion of 10^{-5} mΩcm. An electric field criterion of 1 μV/cm is used to estimate J_c.

Magnetic measurements

Magnetization measurements were performed on the rectangular-shaped sample using a superconducting quantum interference device magnetometer [SQUID VSM, (MPMS3) Quantum Design]. The temperature dependence of susceptibility was measured with a magnetic field of 1 mT applied parallel to the ab-plane. Magnetic J_c was determined using the Bean model from the field dependence of magnetization curves.

Results

Microstructure

As revealed by structural characterization using X-ray diffraction, K-doped Ba122 was phase-pure and epitaxially grown on CaF_2(001) (Supplementary Fig. S1). To evaluate the nanostructure of the grain boundaries, a cross section was observed by scanning transmission electron microscopy (STEM, Fig. 1a) and analyzed by TEM-based scanning PED. The incident direction of the electron beam is approximately parallel to the [110] direction of the CaF_2(001) substrate. An annular dark-field (ADF) image in Fig. 1a shows columnar grains growing in the *z* direction, which is more clearly seen in a virtual dark-field image of the 008 reflection (Fig. 1b). The width of columnar grains is 30–60 nm. The epitaxial relationship is revealed as (001)[110]K-doped Ba122 || (001)[100]CaF_2 by the PED patterns (Fig. 1c, d), which is consistent with the structural characterization by X-ray diffraction (Supplementary Fig. S1). Crystal rotations of K-doped Ba122 around the *b*-axis (equivalent to the *a*-axis) and the *c*-axis were calculated from the crystal orientation data separately and are plotted as two-dimensional maps in Fig. 1e, f. For clarity, the crystal rotation angles β (around the *b*- and *a*-axis) and γ (around the *c*-axis) with respect to CaF_2 are shown in Fig. 1g, h. As clearly seen in the line profiles (Fig. 1i), the average grain rotation around the *b*- (or *a*-) axis is $\Delta\beta_{\text{average}} = 1.5°$ and around the *c*-axis is $\Delta\gamma_{\text{average}} = -1°$ with respect to the ideal values (i.e., $\Delta\beta = \beta - \beta_{\text{ideal}}$, where β_{ideal} is 0°, and $\Delta\gamma = \gamma - \gamma_{\text{ideal}}$, where γ_{ideal} is 45°), resulting in the formation of LAGB networks. As seen in Supplementary Fig. S2, the [001] of K-doped Ba122 was tilted toward $[0\bar{1}0]$ in our coordinate system. The distribution of β over the 2880 points shows that a large fraction is located between 0° and 3.5° with a peak of 1.5° (Supplementary Fig. S2). For completeness, the distribution of γ is also shown in Supplementary Fig. S3. This fact reflects the angular dependence of J_c measurements, which will be discussed later.

Resistivity measurements

$T_{c,90}$, defined as 90% of the normal state resistivity, of our K-doped Ba-122 thin film is 35.2 K (Supplementary Fig. S4). The zero-resistivity temperature $T_{c,0}$ is 33 K, corresponding to the onset temperature of the diamagnetic signal measured by the temperature dependence of susceptibility. Therefore, the transition width, defined as $T_{c,90}$–$T_{c,0,}$ is 2.2 K.

To determine the upper critical field H_{c2} and the irreversibility field H_{irr}, the temperature dependence of resistivity was measured in the field up to 16 T (Fig. 2a, b). As the applied magnetic field increases, a clear shift of T_c to lower temperatures together with a broadening of the superconducting transition is observed for both main crystallographic orientations. The broadening of the transition is more obvious for $H||c$ than $H||ab$; however, such broadening is not as significant compared with

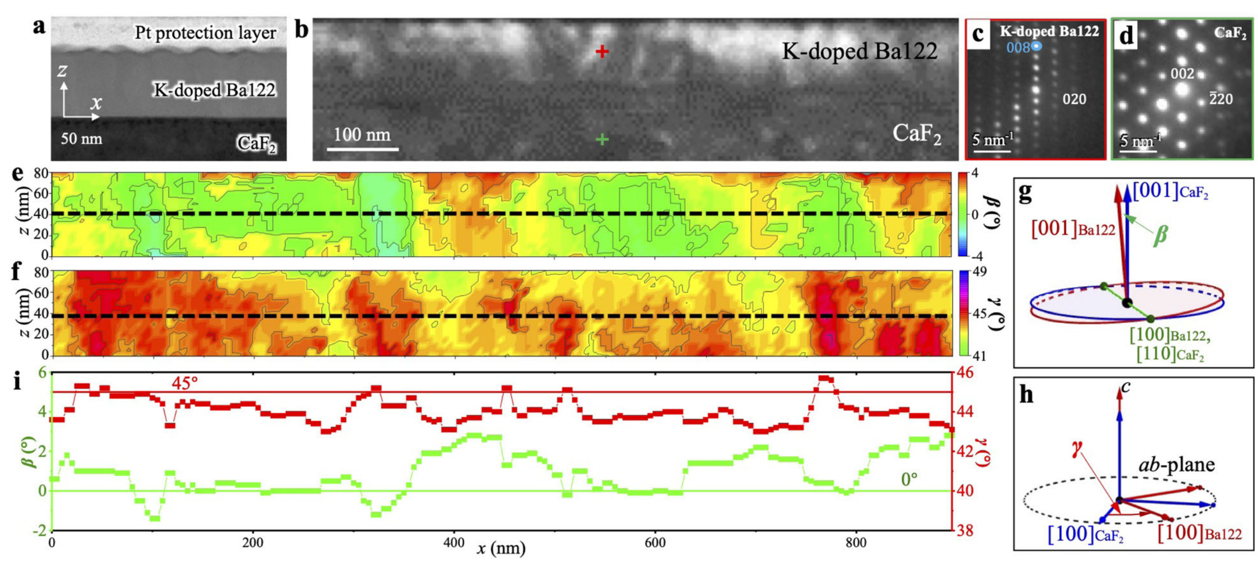

Fig. 1 Microstructural analyses by TEM. a Cross-sectional view obtained by ADF-STEM. **b** Virtual dark-field image of the 008 reflection of K-doped Ba122. **c** Typical PED patterns extracted from the K-doped Ba122 thin film (red cross in **b**) and (**d**), the CaF_2 substrate (green cross in **b**). **e** β rotation map and (**f**), γ rotation map obtained from the K-doped Ba122 thin film. The *z*-axis shows the distance from the interface between K-doped Ba122 and CaF_2, the same direction as shown in **a**. The ideal angles, 0° and 45°, are defined as light-green and red color in (**e**) and (**f**), respectively. **g** Schematic illustrations of the crystal rotation angles β (around the [100]-axis) and (**h**) and γ (around the [001]-axis) with respect to CaF_2 as the reference. **i** Line profiles of β rotation and γ rotation extracted along the black broken lines in (**e**) and (**f**), respectively. The lines of $\beta = 0°$ and $\gamma = 45°$ are marked for comparison.

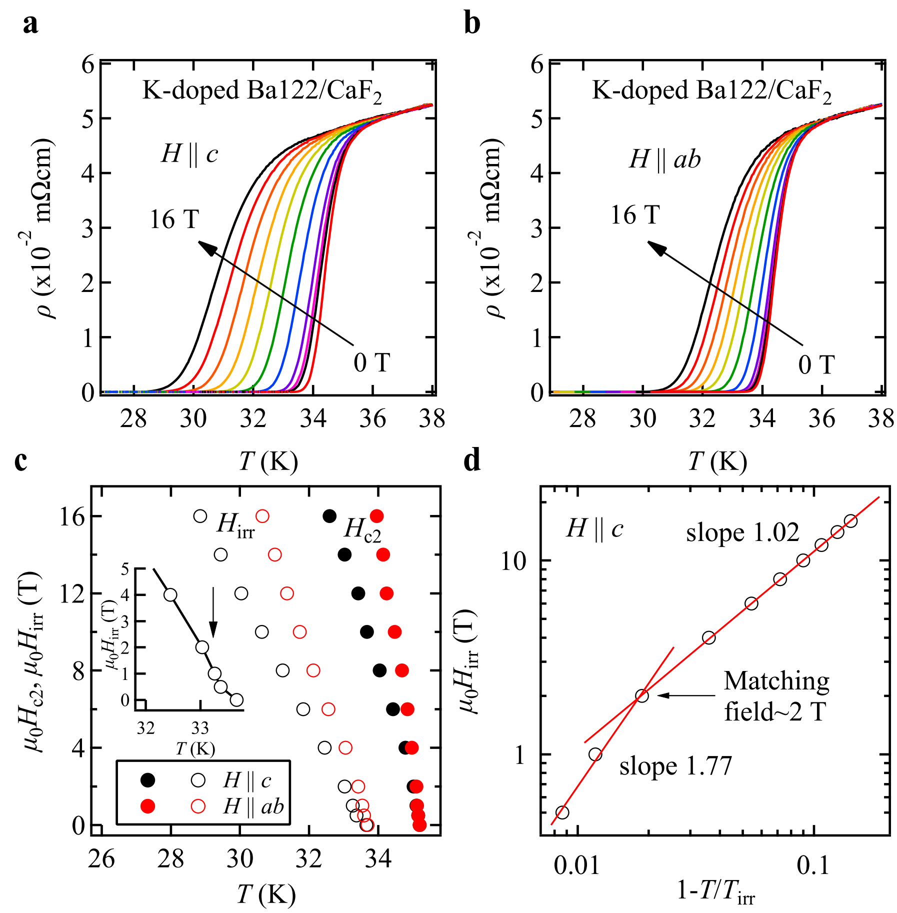

Fig. 2 In-field resistivity measurements and the magnetic phase diagram for the K-doped Ba122 thin film. a Resistivity curves for H parallel to the crystallographic c-axis and (**b**) $H||ab$-plane. The field increment was 2 T from 2 to 16 T. Below 2 T, measurements were conducted at 0, 0.5, 1, and 2 T. **c** Both H_{c2} and H_{irr} are plotted as a function of temperature. The solid symbols represent H_{c2}, and the open symbols show H_{irr}. For $H||c$, the slope of H_{irr} changes by approximately 2 T, as indicated by the arrow. **d** Logarithmic presentation of H_{irr} vs. $1-T/T_{irr}$, where T_{irr} is the irreversibility temperature at the self-field. The slope changes at 2 T, corresponding to the matching field.

*Ln*FeAsO[21] due to the weak thermal fluctuation. It is also worth mentioning that the foot structure in the vicinity of zero resistance arising from the presence of high-angle GBs, previously observed in ref. [22], is not present here. Such a foot structure is also due to poor connectivity. The temperature dependence of the upper critical field H_{c2} and the irreversibility field H_{irr} are summarized in Fig. 2c. The slopes of H_{c2} in the field range $0 \leq \mu_0 H \leq 2$ T are -20.1 TK^{-1} and -11.5 TK^{-1} for $H||ab$ and $||c$, respectively. These values are much higher than those of a single crystal[23]. Another feature is that the slope of the H_{irr}–line for $H||c$ changes at approximately 2 T (inset of Fig. 2c), which is reminiscent of $RE\mathrm{Ba_2Cu_3O_7}$ (*RE*: rare earth elements, *RE*BCO) thin films with *c*-axis correlated defects[24]. To identify the matching field, $\mu_0 H_{irr}$ is plotted as a function $1-T/T_{irr}$, where T_{irr} is the irreversibility temperature (Fig. 2d). The slope of the $\mu_0 H_{irr}$-line changes from 1.77 to 1.02 at 2 T.

Pinning potential

To obtain the activation energy U_0 for vortex motion at given fields, linear fits of the Arrhenius plots for the resistivity curves are conducted (Fig. 3a, b). Based on the thermally activated flux-flow model[25], the slope of the linear fits corresponds to $-U_0$. In fact, on the assumption of the linear temperature dependence, $U(T,H) = U_0(H)(1-T/T_c)$, the following two formulae, $\ln\rho(T,H) = \ln\rho_0(H) - U_0(H)/T$ and $\ln\rho_0(H) = \ln\rho_{0f} + U_0(H)/T_c$, (derived from $\rho(T,H) = \rho_{0f}\exp[-U(T,H)/T] = \rho_{0f}\exp[-U_0(H)(1-T/T_c)/T]$), are obtained with ρ_{0f} being the pre-factor. As seen in Fig. 3c, the activation energy U_0 for both $H||c$ and $||ab$ shows the same power law relation $H^{-\alpha}$ in low fields up to 2 T: the exponent α is ~0.05–0.07, which indicates that single vortex pinning prevails. In this regime, U_0 for both directions is 12,000–13,000 K, whereas the respective values of the $\mathrm{Ba_{0.72}K_{0.28}Fe_2As_2}$ single crystal with $T_c = 32$ K (i.e., underdoped sample) for $H||ab$ and $||c$ at 1 T

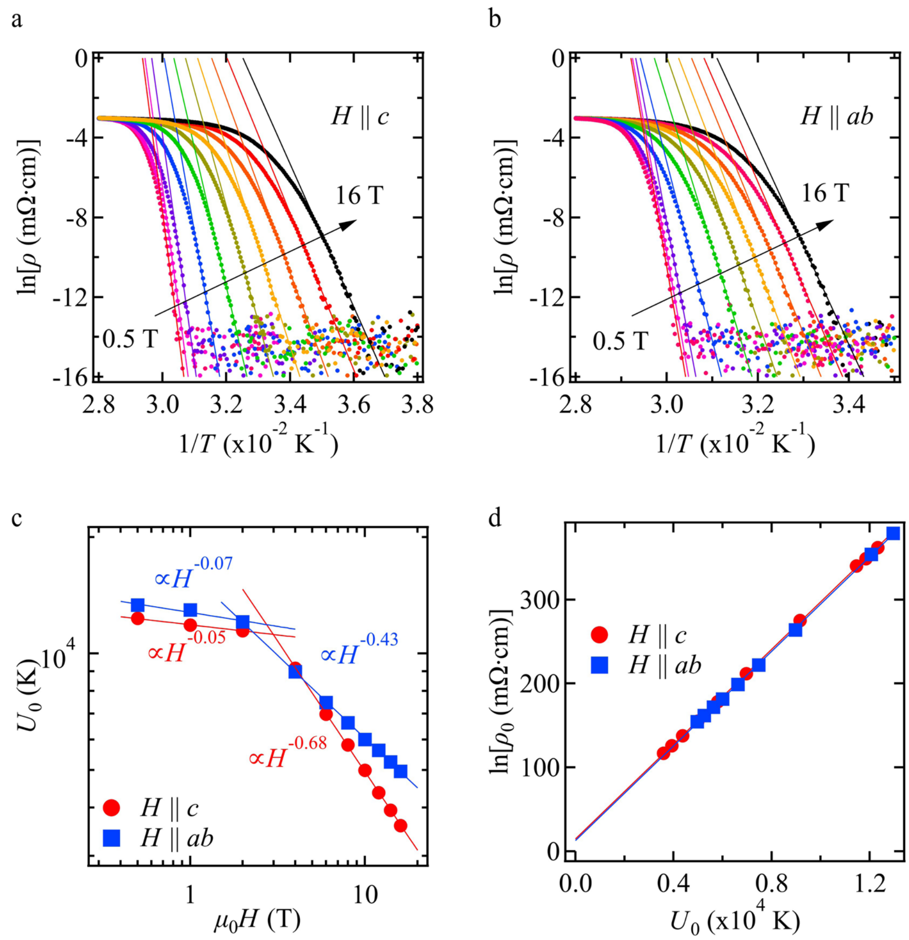

Fig. 3 Arrhenius plots of the resistivity curves shown in Fig. 2a, b and the resultant pinning potential U_0 and prefactor ρ_{0f} for the K-doped Ba122 thin film. a For H parallel to the crystallographic c-axis and (**b**) ab-plane. **c** Field dependence of the pinning potential $U_0(H)$ for both main crystallographic orientations. **d** $U_0(H)$ dependence of ln[ρ_0 (mΩ cm)] for $H||c$ and $||ab$.

are 8500 K and 5000 K[26]. Above 2 T, for $H||ab$, α ~0.5 is consistent with a plastic pinning regime[27]. On the other hand, for $H||c$, α is 0.68, which is located between 0.5 and 1, where the exponent α = 1 is the theoretical prediction for collective pinning[28]. It is interesting to note that for the high field regime (i.e., 13–16 T) U_0 of our film is comparable to that of single crystals[26].

The relationship between ln[ρ_0] and U_0 for both orientations is shown in Fig. 3d, where the slope of the linear fits corresponds to $1/T_c$. The respective T_c for $H||c$ and $||ab$ are 35.4 K and 35.5 K, which is close to $T_{c,90}$. This perfect scaling justifies the initial assumption of $U(T, H) = U_0(H)(1-T/T_c)$ in a wide range of temperatures.

Field dependence of J_c obtained from the transport and magnetization measurements

Figure 4a shows the in-field J_c properties for the K-doped Ba122 thin film measured by the I–V (or current density J—electric field E) characteristics at various temperatures. E–J curves for $H||c$ are shown in Supplementary Fig. S5. At 30 K for both $H||c$ and $||ab$, J_c gradually decreases with increasing fields. However, J_c below 25 K is almost insensitive to applied magnetic fields, and a high J_c above 2×10^5 A cm^{-2} is maintained over the entire investigated field range. The most striking feature is that J_c for $H||c$ exceeds that for $H||ab$ with decreasing temperature, opposite to the expected intrinsic behavior related to the anisotropy of H_{c2}. Similar features with inverse anisotropy caused by strong c-axis correlated defects were previously observed, for instance, in Co-doped Ba122[29] and *RE*BCO[24,30,31]. These results infer that strong c-axis pinning is active at $T \leq$ 25 K. It is worth mentioning that the J_c peak for $H||c$ is prominent at high temperatures for *RE*BCO, but it is strongly suppressed with decreasing temperature[32], which is different from FBS.

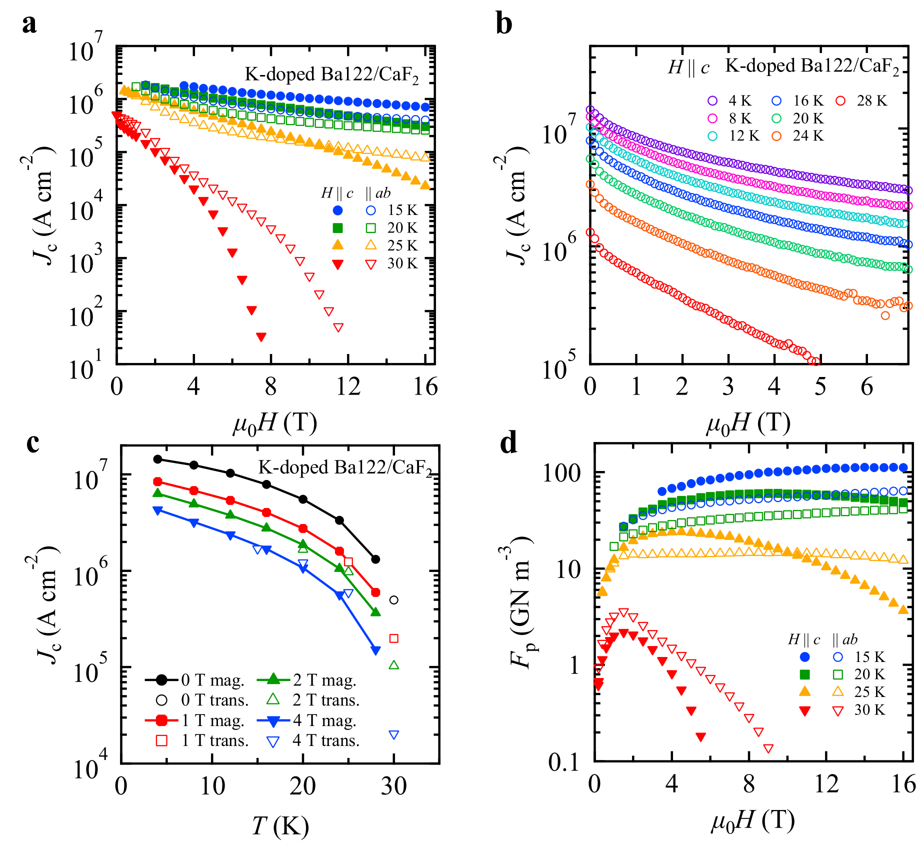

Fig. 4 Field dependence of the critical current density J_c measured by the transport and magnetization methods. a J_c-H characteristics for both main orientations obtained from the transport measurements. The solid symbols represent $H || c$, and the open symbols show $H||ab$. **b** Field dependence of J_c evaluated from the magnetization measurements using the extended Bean model. **c** Temperature dependence of J_c for several applied fields $H||c$. **d** Field dependence of F_p calculated from (**a**).

To prevent overheating of the contact leads/pads and possible sample damage, the E–J characterization was limited at low fields and temperatures. Hence, for completeness, the field dependence of magnetization to extract J_c was measured on a rectangular sample cut from the same film used for transport measurements over a wider temperature range (Supplementary Fig. S6). J_c calculated from the Bean model is shown in Fig. 4b. Except for 28 K, J_c has a weak field dependence, which is consistent with the transport J_c. At 4 K, self-field J_c reaches 14.4 MA cm^{-2}, corresponding to ~9% of the depairing current density J_d[16]. The temperature dependence of J_c measured by electrical transport measurements well follows the magnetization J_c (Fig. 4c), although the electric field criterion E_c of the former is higher than that of the latter. The data at 30 K slightly deviating from the trend are likely due to the fluctuations close to T_c.

The field dependence of F_p calculated from Fig. 4a is summarized in Fig. 4d. Because of the presence of strong c-axis pinning at $T \leq$ 25 K, the maximum F_p is always recorded for $H||c$ within our experimental condition (i.e., up to 16 T).

Angle dependence of J_c obtained from the transport measurement

To obtain a better understanding of the pinning efficiency, measurements of the angular dependences of J_c were conducted at various temperatures and field strengths (Fig. 5). For all fields, the J_c peaks around $H||c$ ($\theta = 90°$) are weak at 30 K; however, they become intense at $T \leq$ 25 K. The peak position of J_c around $H||c$ is ~4° away from the c-axis, indicating that "the correlated defects" are slightly tilted. This is because the columnar grains of K-doped Ba122, which creates LAGBs along the grains, grew unidirectionally at an incline of a few degrees with respect to the substrate normal. To clearly see the effect of correlated defects on J_c, J_c anisotropy defined as J_c/J_c^{ab}, where J_c^{ab} is J_c at $\theta =$ 180°, is plotted at the fixed magnetic field (Fig. 5e–g). The black dashed lines are positioned at 94° to clearly see the J_c peaks. At 4 T and 30 K, J_c/J_c^{ab} is approximately 0.5 for $H||c$ (Fig. 5e), increasing to ~1.6 at low temperatures. This is a clear indication that the strong pinning around $H||c$ is activated between 30 and 25 K. As increasing applied magnetic fields, a full evolution of

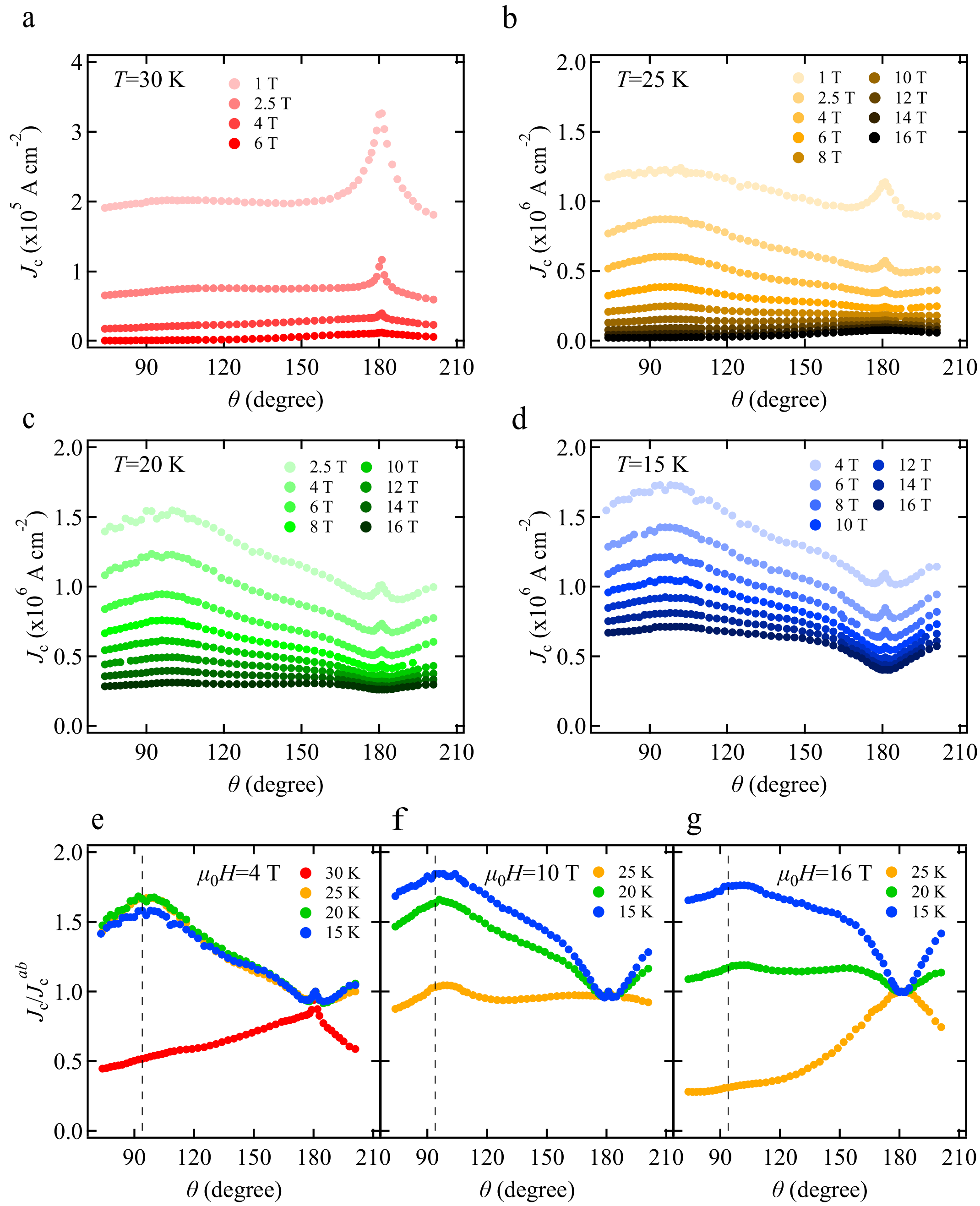

Fig. 5 Angular dependence of transport J_c for the K-doped Ba122 thin film. The measurement temperatures were (**a**), 30 K, (**b**), 25 K, (**c**), 20 K, and (**d**), 15 K. Angles of $\theta = 90°$ and 180° correspond to $H||c$ and $||ab$, respectively. Angle dependence of J_c normalized by J_c for $H||ab$ (J_c^{ab}) measured at (**e**) 4 T, (**f**) 10 T, and (**g**) 16 T. The dashed lines are located at $\theta = 94°$ to clearly see the J_c peaks.

the angular dependence of J_c/J_c^{ab} can be observed from a roughly regular behavior with a maximum at 180° for $H||ab$ (e.g., 16 T and 25 K) to an almost isotropic behavior (e.g., 10 T and 25 K as well as 16 T and 20 K) and finally to a behavior strongly affected by *c*-axis correlated pinning at the lowest temperatures.

Discussions

Through microstructural analyses and electrical transport measurements, a "*c*-axis correlated defect" in our K-doped Ba122 thin film is identified as a low-angle grain boundary (LAGB). On the assumption that the mean distance *d* of correlated pinning is identical to that of the width of K-doped Ba122 grains (i.e., 30–60 nm), the matching field $B_\phi \sim \phi_0/d^2$ is approximately 2 T at which a kink of H_{irr} is observed (Fig. 2c, d, ϕ_0 being the flux quantum). As shown in Fig. 5, this pinning is strongly temperature dependent, which is presumably due to the crossover between the in-plane coherence length of K-doped Ba122 and the defect size. The correlated GB pinning and networks improve not only self-field J_c but also in-field J_c for H close to the c-axis. Consequently, the anisotropy of J_c is inverted with respect to H_{c2}. A similar observation was reported in ref. [33], where the GBs between columnar grains in MgB_2 thin films grown by e-beam evaporation worked as pinning centers.

The tilted growth of K-doped Ba122 is presumably due to the geometrical configuration of the deposition sources together with the deposition without rotating substrates. In our setup, vapor flux arrives at the substrate with an oblique angle. Additionally, adatoms are expected to diffuse relatively slowly on the substrate, since the substrate temperature was low compared with the incongruent melting and decomposition temperatures of K-doped Ba122 (917 °C and 988 °C, respectively)[34]. Hence, the shadowing effect[35], which limits the formation of new nuclei during the deposition behind initially formed nuclei, is pronounced, resulting in inclined columnar growth.

A pinning force density F_p of 114 GN m^{-3} is recorded even at 15 K and 14–16 T (obtained from the transport measurement) and exceeds 200 GNm^{-3} at 4 K and a field above 6 T (the data at 4 K are obtained from the magnetization measurements in Fig. 4b). In Fig. 6, the field dependence of F_p for our K-doped Ba122 thin film is plotted. For comparison, we also plotted the following data of pinning-enhanced Ba122 single crystal and thin films with different dopants: K-doped Ba122 single crystal with Pb-ion irradiation measured at 5 K[17], Co-doped Ba122 thin film with large amounts of stacking faults measured at 4.2 K[35], Co-doped Ba122 thin film with 3 mol % $BaZrO_3$ (BZO) measured at 5 K[36], and P-doped Ba122 with 3 mol% BZO measured at 4.2 K and 15 K[37]. As seen, up to 4 T, the F_p of our K-doped Ba122 thin film is the highest among the pinning-enhanced Ba122. Although the F_p data above 7 T are missing, the extrapolated value at 9 T for the K-doped Ba122 thin film is comparable to the highest value reported for the Co-doped Ba122 thin film.

The large improvement of the superconducting properties of our K-doped Ba122 thin film without APCs is due to the high density of correlated pinning centers created by LAGB networks. Unlike Co- and P-doped Ba122 thin films, the growth temperature of K-doped Ba122 thin film is quite low (~400 °C). This low-temperature synthesis may lead to a small grain size and hence an increase in the density of LAGBs. It is worth

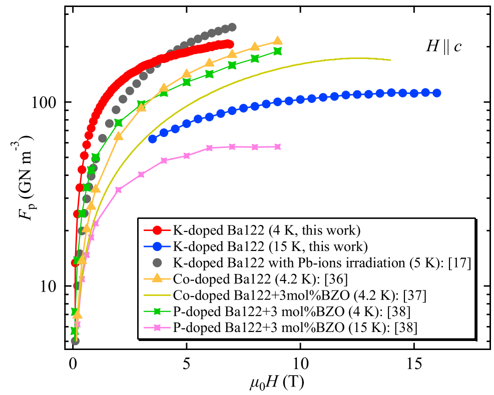

Fig. 6 Field dependence of the pinning force density F_p for $H||c$. The F_p for K-doped Ba122 thin film measured at 4 K and 15 K. The respective F_p at 4 K and 15 K are calculated using the J_c–H data obtained from the magnetic and transport measurements. For comparison, the data of K-doped Ba122 single crystal with Pb-ion irradiation measured at 5 K[17], Co-doped Ba122 thin film with a large number of stacking faults measured at 4.2 K[36], Co-doped Ba122 thin film with 3 mol% $BaZrO_3$ (BZO) measured at 4.2 K[37], and P-doped Ba122 thin film with 3 mol% BZO measured at 4 K and 15 K[38] are also plotted.

mentioning that the dislocation density increases with increasing grain boundary angle. Hence, further improvement of in-field J_c is possible by enlarging the texture spread within the critical angle θ_c. The grain boundary engineering presented in this study highlights a possible novel approach to improve the superconducting properties, which is a simple and industrially scalable manner.

Conclusion

Herein, we investigated the nanoscale microstructure of a K-doped Ba122 epitaxial thin film grown on CaF_2 by molecular beam epitaxy. The nanoscale crystal orientation mapping shows that the film is composed of columnar grains with widths of approximately 30–60 nm. The average grain rotation around the b- (or a-) axis is 1.5° and around the c-axis is −1° with respect to the ideal values, resulting in the formation of low-angle grain boundary networks. LAGB networks are used to realize superior superconducting properties of K-doped Ba122: the pinning force density F_p for $H||c$ exceeds 200 GN m^{-3} at 4 K and above 6 T, which is comparable to the best performing K-doped Ba122 by ion irradiation.

Acknowledgements
The authors thank Wai-Kwong Kwok (Argonne National Laboratory) for data[17], Yanwei Ma (Chinese Academy of Science) for data[36], Jongmin Lee and Sanghan Lee (Gwangju Institute of Science and Technology) for data[37], and Masashi Miura (Seikei University) for data[38]. This work was supported by JST CREST Grant Number JPMJCR18J4. A portion of the work was performed at the National High Magnetic Field Laboratory, which was supported by National Science Foundation Cooperative Agreement No. DMR-1644779 and the State

of Florida. It was also supported by the US Department of Energy Office of High Energy Physics under grant number DE-SC0018750. This work was also partly supported by the Advanced Characterization Platform of the Nanotechnology Platform Japan sponsored by the Ministry of Education, Culture, Sports, Science and Technology (MEXT), Japan.

Author details

[1]Department of Materials Physics, Nagoya University, Furo-cho, Nagoya 464–8603, Japan. [2]JST CREST, Kawaguchi, Saitama 332–0012, Japan. [3]Department of Applied Physics, Tokyo University of Agriculture and Technology, Koganei, Tokyo 184–8588, Japan. [4]Applied Superconductivity Center, National High Magnetic Field Laboratory, Florida State University, Tallahassee, FL, USA. [5]The Ultramicroscopy Research Center, Kyushu University, 744 Motooka, Nishi, Fukuoka 819–0395, Japan. [6]Interdisciplinary Graduate School of Engineering Sciences, Kyushu University, Kasuga, Fukuoka 816–8580, Japan. [7]Institute for Materials Chemistry and Engineering, Kyushu University, Kasuga, Fukuoka 816–8580, Japan

Author contributions

K.I. and A.Y. designed the study. K.I. and C.T. wrote manuscript together with D. Q., H.S., S.H., M.N., and A.Y. Thin film preparation, structural characterization by XRD, and micro bridge fabrication were carried out by D.Q., M.N., K.I., T.H., and C.T. Microstructural characterization by TEM was performed by C.W., Z.G., H.G., H.S., and S.H., and C.T. conducted in-field electrical transport measurements.

Conflict of interest

The authors declare no competing interests.

Publisher's note

Springer Nature remains neutral with regard to jurisdictional claims in published maps and institutional affiliations.

Supplementary information The online version contains supplementary material available at https://doi.org/10.1038/s41427-021-00337-5.

Received: 8 May 2021 Revised: 20 August 2021 Accepted: 3 September 2021
Published online: 22 October 2021

References

1. Hiramatsu, H., Katase, T., Kamiya, T. & Hosono, H. Thin film growth and device fabrication of iron-based superconductors. *J. Phys. Soc. Jpn.* **81**, 011011 (2012).
2. Li, Q., Si, W. & Dimitrov, I. K. Films of iron chalcogenide superconductors. *Rep. Prog. Phys.* **74**, 124510 (2011).
3. Iida, K., Hänisch, J. & Tarantini, C. Fe-based superconducting thin films on metallic substrates: Growth, characteristics, and relevant properties. *Appl. Phys. Rev.* **5**, 031304 (2018).
4. Sakoda, M., Iida, K. & Naito, M. Recent progress in thin film growth of Fe-based superconductors: superior superconductivity achieved by thin films. *Supercond. Sci. Technol.* **31**, 093001 (2018).
5. Hänisch, J., Iida, K., Hühne, R. & Tarantini, C. Fe-based superconducting thin films-preparation and tuning of superconducting properties. *Supercond. Sci. Technol.* **32**, 093001 (2019).
6. Qin, D. et al. A. Realization of epitaxial thin films of the superconductor K-doped $BaFe_2As_2$. *Phys. Rev. Mater.* **5**, 014801 (2021).
7. Iida, K., Hänisch, J. & Yamamoto, A. Grain boundary characteristics of Fe-based superconductors. *Supercond. Sci. Technol.* **33**, 043001 (2020).
8. Hänisch, J. & Iida, K. *Superconductivity From Materials Science to Practical Applications* 269–302, ch 10 (Springer, 2020).
9. Katase, T. et al. Biaxially textured cobalt-doped $BaFe_2As_2$ films with high critical current density over 1 MA/cm^2 on MgO-buffered metal-tape flexible substrates. *Appl. Phys. Lett.* **98**, 242510 (2011).
10. Sato, H., Hiramatsu, H., Kamiya, T. & Hosono, H. Enhanced critical-current in P-doped $BaFe_2As_2$ thin films on metal substrates arising from poorly aligned grain boundaries. *Sci. Rep.* **6**, 36828 (2016).
11. Xu, Z., Yuan, P., Fan, F., Chen, Y. & Ma, Y. Transport properties and pinning analysis for Co-doped $BaFe_2As_2$ thin films on metal tapes. *Supercond. Sci. Technol.* **31**, 055001 (2018).
12. Iida, K. et al. High-field transport properties of a P-doped $BaFe_2As_2$ film on technical substrate. *Sci. Rep.* **7**, 39951 (2017).
13. Fang, L. et al. Huge critical current density and tailored superconducting anisotropy in $SmFeAsO_{0.8}F_{0.15}$ by low-density columnar-defect incorporation. *Nat. Commun.* **4**, 2655 (2013).
14. Taen, T., Ohtake, F., Pyon, S., Tamegai, T. & Kitamura, H. Critical current density and vortex dynamics in pristine and proton-irradiated $Ba_{0.6}K_{0.4}Fe_2As_2$. *Supercond. Sci. Technol.* **28**, 085003 (2015).
15. Takahashi, A. et al. Effects of splyaed columnar defects on critical current density in $CaKFe_4As_4$. *J. Phys.: Conf. Ser.* **1590**, 012015 (2020).
16. Mishev, V., Nakajima, M., Eisaki, H. & Eisterer, M. Effects of introducing isotropic artificial defects on the superconducting properties of differently doped Ba-122 based single crystals. *Sci. Rep.* **6**, 27783 (2015).
17. Fang, L. et al. High, magnetic field independent critical currents in $(Ba,K)Fe_2As_2$ crystals. *Appl. Phys. Lett.* **101**, 012601 (2012).
18. Rauch, E. F. et al. Automated nanocrystal orientation and phase mapping in the transmission electron microscope on the basis of precession electron diffraction. *Z. Kristallogr.* **225**, 103–109 (2010).
19. Zaikina, J. V. et al. Facile synthesis of $Ba_{1-x}K_xFe_2As_2$ superconductors via hydride route. *J. Am. Chem. Soc.* **136**, 16932–16939 (2014).
20. Cheetham, A. K., Fender, B. E. F. & Cooper, M. J. Defect structure of calcium fluoride containing excess anions I. Bragg scattering. *J. Phys. C.* **4**, 3107–3121 (1971).
21. Jaroszynski, J. et al. Upper critical fields and thermally-activated transport $NdFeAsO_{0.7}F_{0.3}$ single crystal. *Phys. Rev. B* **78**, 174523 (2008).
22. Lee, N., Jung, S.-G., Kim, D. & Kang, W. Potassium-doped $BaFe_2As_2$ superconducting thin films with a transition temperature of 40 K. *Appl. Phys. Lett.* **96**, 202505 (2010).
23. Ishida, S. et al. Doping-dependent critical current properties in K, Co, and P-doped $BaFe_2As_2$ single crystals. *Phys. Rev. B* **95**, 014517 (2017).
24. Horide, T. et al. Influence of matching field on critical current density and irreversibility temperature in $YBa_2Cu_3O_7$ films with $BaMO_3$ (M=Zr, Sn, Hf) nanorods. *Appl. Phys. Lett.* **108**, 082601 (2016).
25. Palstra, T. T. M., Batlogg, B., Schneemeyer, L. F. & Waszczak, J. V. Thermally activated dissipation in $Bi_{2.2}Sr_2Ca_{0.8}Cu_2O_{8+\delta}$. *Phys. Rev. Lett.* **61**, 1662–1665 (1989).
26. Wang, X.-L. et al. Very strong intrinsic flux pinning and vortex avalanches in $(Ba,K)Fe_2As_2$ superconducting single crystals. *Phys. Rev. B* **82**, 024525 (2010).
27. Geshkenbein, V., Larkin, A., Feigel'man, M. & Vinokur, V. Flux pinning and creep in high-T_c superconductors. *Phys. C.* **162-164**, 239–240 (1989).
28. Blatter, G., Feigel'man, M. V., Geshkenbin, V. B., Larkin, A. I. & Vinokur, V. M. Vortices in high-temperature superconductors. *Rev. Mod. Phys.* **66**, 1125–1388 (1994).
29. Tarantini, C. et al. Strong vortex pinning in Co-doped $BaFe_2As_2$ single crystal thin films. *Appl. Phys. Lett.* **96**, 142510 (2010).
30. Matsui, H. et al. 4-fold enhancement in the critical current density of $YBa_2Cu_3O_7$ films by practical ion irradiation. *Appl. Phys. Lett.* **101**, 232601 (2012).
31. Opherden, L. et al. Large pinning forces and matching effects in $YBa_2Cu_3O_{7-\delta}$ thin films with $Ba_2Y(Nb/Ta)O_6$ nano-precipitates. *Sci. Rep.* **6**, 21188 (2016).
32. Xu, A. et al. Broad temperature pinning study of 15 mol.% Zr-added (Gd,Y)-Ba-Cu-O MOCVD coated conductors. *IEEE Trans. Appl. Supercond.* **25**, 6603105 (2015).
33. Kitaguchi, H. et al. MgB_2 films with very high critical current densities due to strong grain boundary pinning. *Appl. Phys. Lett.* **85**, 2842–2844 (2004).
34. Sun, G. L. et al. Single crystal growth and effect of doping on structural, transport and magnetic properties of $A_{1-x}K_xFe_2As_2$ (A=Ba, Sr). *J. Supercond. Nov. Magn.* **24**, 1773–1785 (2011).
35. Dirks, A. G. & Leamy, H. J. Columnar microstructure in vapor-deposited thin films. *Thin Solid Films* **47**, 219–233 (1977).
36. Yuan, P. et al. Vortex pinning properties in Co-doped $BaFe_2As_2$ thin films with a high critical current density over 2 MA cm^{-2} at 9 T. *Supercond. Sci. Technol.* **30**, 025001 (2016).
37. Lee, J. et al. High critical current density over 1 MAcm^{-2} at 13 T in $BaZrO_3$ incorporated $Ba(Fe,Co)_2As_2$ thin film. *Supercond. Sci. Technol.* **30**, 085006 (2017).
38. Miura, M. et al. Enhanced critical current density in $BaFe_2(As_{0.66}P_{0.33})_2$ nanocomposite superconducting films. *Supercond. Sci. Technol.* **32**, 064005 (2019).